Residual GNSS Ionospheric Error Analysis in Future Low Earth Orbit Applications

Can Oezmaden*, Sarah Pelzer*, Omar García Crespillo†,
Marius Brachvogel*, Michael Niestroj* and Michael Meurer*†
* *Chair of Navigation, RWTH Aachen University, Aachen, Germany*
† *Institute of Communications and Navigation, German Aerospace Center (DLR), Oberpfaffenhofen, Germany*
Email: can.oezmaden@nav.rwth-aachen.de

***Abstract*—Future low Earth orbit (LEO) applications such as LEO positioning, navigation, and timing (PNT) and LEO-based monitoring of global navigation satellite systems (GNSS) are expected to experience a residual ionospheric delay depending on the altitude a constellation would be deployed. The ionosphere reaches its peak concentration in the F-region at and altitude of 300 km to 400 km. The concentrations of charged particles beyond this altitude constitute the topside ionosphere and may contain a non-negligible density as high up as 1000 km. The literature on dealing with the residual ionospheric error is scarce, and the impact of the residual error has not been yet studied thoroughly in the context of future LEO applications. In this paper we aim to quantify and analyze this residual error. We aid our analysis with 3D-ionospheric model estimates and compare them to collected in-situ total electron content (TEC) measurements from LEO. Thus, we aim to characterize the expected uncorrected error magnitude and its distribution for a single-frequency GNSS receiver depending on the LEO altitude, and on the solar and geomagnetic activity.**

***Index Terms*—ionosphere, low Earth orbit, GNSS, LEO PNT, LEO-based GNSS monitoring**

I. Introduction

Recent years have shown a steady growth in the deployment of low Earth orbit (LEO) satellites, partly thanks to the rise of so-called LEO megaconstellations providing telecommunication and broadband internet access services. The move towards LEO has triggered institutional and commercial interest in investigating the benefits of low Earth orbit constellations in the context of positioning, navigation, and timing (PNT).

The goal in LEO PNT is to diversify the existing global navigation satellite systems (GNSS) by either using existing satellites in LEO, such as Starlink, Iridium, and OneWeb [1]; or by launching dedicated LEO constellations with tailored signals in a variety of bands as summarized by Eissfeller et al. [2]. The latter is now being attempted by, amongst others, ESA [3], Xona [4] and TrustPoint [5].

LEO PNT constellations offer important advantages in the context of emerging autonomous applications requiring precise positioning. They offer a rapid change in geometry, which on one hand lowers the convergence time of precise point positioning (PPP) [6]; and on the other, provides a potential for higher availability due to less time spent occulated behind high-rise building in urban environments [4]. A further potential added value of such LEO constellations is providing integrity monitoring and an augmentation service for GNSS-users. Efforts to investigate this include a collaboration between German Aerospace Center (DLR) and centre national d'études spatiales (CNES) [7], related activities in the Chinese Centispace program [6], and some proposals for the BeiDou system as presented by Gao et al. [8]. LEO-based GNSS monitoring systems may offer an augmentation service with significant advantages over existing infrastructure-based counterparts, such as satellite-based augmentation systems (SBAS) and ground-based augmentation systems (GBAS). As identified by García Crespillo et al. [9], these can include:

- global coverage,
- reduced dependency on costly ground-based infrastructure,
- potentially a lower time to alert (TTA),
- lower minimum detectable biases (MDB),
- a more direct measurement of the signal-in-space (SiS).

The latter is true since atmospheric effects, such as the tropospheric error, can be neglected at LEO, whereas the ionospheric error is diminished due to a thinner residual layer of the ionosphere above most low Earth orbits.

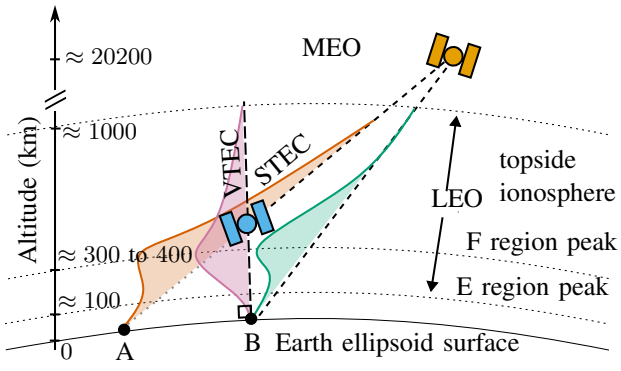

Fig. 1. Conceptual sketch of the different ionospheric slant paths. The GNSS satellite is depicted above in MEO in orange. Its signal is being received by the LEO satellite in blue. The slant total electron content that affects this signal is sketched from point A as the orange distribution. The slant total electron content from point B, the satellite's projected Earth position, is sketched in green. The vertical total electron content distribution from satellite's projected Earth position B is sketched in magenta.

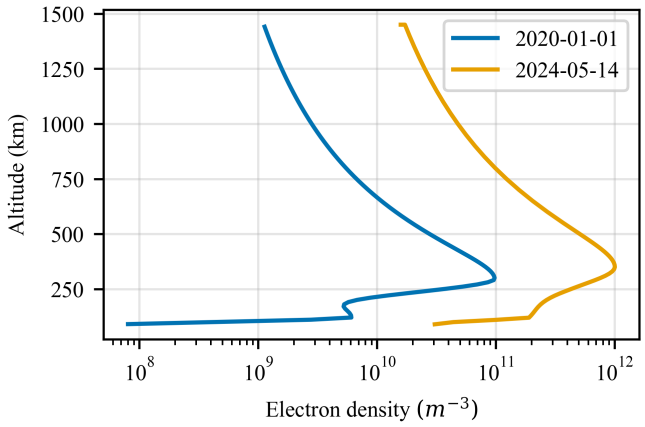

Fig. 2. Visualization of the electron density concentration over LEO altitudes vertically above Aachen, Germany (50.78°N, 6.07°E). Blue line represents the density distribution on January 1st, 2020 (solar low). Orange line visualizes May 11th, 2024. This day marked and extreme solar storm and geomagnetic event. F-region peak is situated visible higher, and the topside ionosphere is ionized by an order of magnitude more compared to solar low. Modelled using NeQuick-2 and historical solar flux data.

The two outlined applications are not exhaustive and not mutually exclusive either, meaning LEO PNT systems can also be used as LEO-based GNSS monitoring systems. Regardless of the end goal, all future LEO applications are expected to utilize one or more GNSS receivers onboard. The GNSS signal measurements and observables will be used on one hand to support the precise obit determination and time synchronization (ODTS), and on the other hand as a source for various GNSS monitors. The performance of satellite monitors may depend on the height of the LEO constellation. There seems to be a wide-range of heights of the planned and existing LEO PNT constellations, ranging from around 500 km to 1500 km. The lower end of this interval roughly coincides with the peak electron density in the F-region of the ionosphere as shown in Figure 2. The concentration of charged particles does not abruptly end after the peak, as the electron content slowly decays radially away from Earth. In the case of high solar and/or geomagnetic activity, the electron density in this topside ionosphere may range up to about 1000 km as also shown in Figure 2. Thus, depending on the height of the LEO satellite a different amount of total electron content (TEC) from the residual topside ionosphere would affect the GNSS signal.

The usual dual-frequency correction applied for the ionospheric delay on the GNSS signal, namely the ionosphere-free (IF) combination, has significant implications in the GNSS monitoring application and thus is not a trivial solution to the problem:

- IF-combination has higher residual noise in the observables, thus worsening the monitoring sensitivity,
- inter-frequency biases cannot be monitored, as carrier phase ambiguities etc. need to be solved in a filter fashion
- anomalies occurring in the signal of one frequency are missed,
- the monitoring capability is severely handicapped should the second frequency of the monitored GNSS signal become unavailable.

The alternative approach using single-frequency carrier-code correction, often called group and phase ionospheric correction (GRAPHIC) [10], disallows the use of snapshot based positioning and/or integrity monitoring, as carrier-phase ambiguities need to be estimated within a filter. It suffers from scaling the carrier-phase noise with a larger pseudorange noise.

This presents a unique challenge for future LEO-based GNSS monitoring applications, since there is a need to model and bound the expected single-frequency residual ionospheric contributions to GNSS observables. User equipment on the ground rely on ionosphere error models that have been designed for applications operating up to the troposphere. Simple, but widely used models, such as Klobuchar [11], take the so-called thin-shell approach. This cannot be applied to a LEO-borne receiver.

A. Relevant literature

Previous work on ionospheric GNSS error modeling in low Earth orbit is scarce. Most literature on the topic focuses on the geophysical interpretation of the phenomena in the topside ionosphere. Various published studies in this field make use of in-situ measurements of the ionosphere from scientific LEO missions to create tomographic imaging of the ionosphere and/or to validate existing empirical models that provide a 3D representation of the ionosphere [12], [13], [14].

Some research explores using the available ground data to estimate the effect of the residual ionosphere at LEO on GNSS signals. Montenbruck and Gill [15] utilize IGS's two-dimensional global ionosphere maps (GIM). The authors combine the vertical TEC (VTEC) value for the projected location on Earth with its respective ionospheric conditions of the day in order to generate a Chapman profile using the International Rerefence Ionosphere (IRI) model IRI95. Similarly, Kim and Kim [16] utilize a newer version of the model, namely IRI07. In both cases, the authors subsequently determine a scale factor dependent on how much of the electron density is distributed above a specific LEO height in relation to the predicted VTEC on ground. Montenbruck and Gill report 90% accuracy and a residual error of around 4 m in pseudorange. The authors validate these findings on data from one day, the 7th of August 2000. Kim and Kim report a deviation in the order of 3.5 TECU between the measured and the estimated VTEC. The authors validate their findings in the timeframe of the year 2004. In both cases, this methodology requires a-priori knowledge of the VTEC distribution on the ground and an appropriate mapping function to convert predicted VTEC into slant TEC (STEC) in order to eliminate the ionospheric error.

Montenbruck and González Rodríguez [17] assess the direct use of NeQuick-G for LEO users. The authors employ techniques to reduce computational load and validate their method on the SWARM dataset using a timeframe of two years by processing one day per month. The reported findings include 87% correction rate for 2014, a year with high solar activity,

and 98% for 2017, a year with low solar activity. Montenbruck and González Rodríguez also find no difference in comparing ground STEC values between a LEO satellite position projected vertically down to Earth (Point A in Figure 1), or a position found by following the slant until it intersects the ground (Point B in Figure 1).

Kim and Kim [18], extend the original methodology in their subsequent work, to receive the VTEC distribution from existing SBAS signals. The scale factor is also revamped to be determined via the NeQuick-G model, by utilizing the three broadcast coefficients parametrizing the effective ionization level. Thus, this methodology would work on LEO satellites without any further data link to the ground. The authors report improvement over direct use of NeQuick-G over the regional area of SBAS. The timeframe of their validation is the year 2015, a year with high solar activity.

Imad et al. [19] develop a novel model for the ionospheric error in the context of LEO PNT. The authors process a timeframe of 11 years, but entirely focus on a ground user receiving both medium Earth orbit (MEO) GNSS and LEO PNT signals. Thus, the residual ionospheric error between the MEO and LEO is left unanswered. Since the work of Montenbruck and Gill was based on only one day of data, or in the case of Montenbruck and González Rodríguez on only one day from various months, and the work of Kim and Kim is restricted to SBAS regional coverage, the development and validation of a global ionospheric model for LEO-borne GNSS receivers remains an open field of study.

B. Contributions of this paper

The aim of our work is to quantify and analyze the residual ionospheric error in GNSS observables in LEO.

Our contributions are as follows:

- we analyze statistics on TEC measurements in LEO gathered over 24 years with an hourly rate,
- we ensure diversity of different states of solar cycles in our data and study the relevant quantities by differentiating nominal and non-nominal ionospheric states,
- we analyze the altitude dependency in our data and study the impact of the altitude of a LEO constellation as a determining factor for the residual ionosphere effect,
- we quantify the discrepancy between 3D-ionosphere models and in-situ data from scientific LEO missions.

II. Ionosphere

The ionosphere consists of layers of charged particles which are located above the Earth in the thermosphere. The maximum concentration of these particles form the so-called F-region, at an altitude of 300 km to 400 km [20], as illustrated in Figures 1 and 2. Another high concentration of charged particles is situated at a lower altitude of around 100 km, forming the peak of the so-called E-region. Since orbits in the E-region decay due to high atmospheric drag, they are not typically considered for LEO constellation deployment. In this paper, we would focus on LEO satellites which are mostly situated just below or above the F-region.

TABLE I
Classification of geomagnetic activity based on Ap-Index

Class. per Cander [21]	Ap Value	Class. in this paper
Quiet	0 to 7	Nominal
Unsettled	8 to 15	Nominal
Active	16 to 29	Non-nominal
Minor Storm	30 to 49	Non-nominal
Major Storm	50 to 99	Non-nominal
Severe Storm	> 100	Non-nominal

Two major factors influencing the state of the ionosphere is the solar radiation and Earth's magnetic field. Depending on the solar and geomagnetic activity, the altitude of the F-region peak might shift, thus causing perturbations in the perceived ionosphere for the LEO satellite. The solar radiation is often expressed by the measurement of the flux $F_{10.7}$ at the wavelength of 10.7 cm. This parameter is often given in solar flux unit (s.f.u.) normalized by $10^{-22}\mathrm{Wm}^{-2}\mathrm{Hz}^{-1}$. The geomagnetic activity of the Earth is described by a multitude of indices, of which the so-called Ap-index is often used to characterize the ionosphere as per Table I.

For LEO-borne receivers, one must assume an unknown amount of electron content situated on a slant path between the LEO satellite and the GNSS satellite. Thus, a 3D model describing this distribution of charged particles is needed at LEO. These models include the aforementioned International Rerefence Ionosphere (IRI), but also the NeQuick family of models. NeQuick-1 has been released in 2005 and has been based on previous work on modeling the ionosphere by Di Giovanni and Radicella [22]. An updated version, namely NeQuick-2, has been released in 2008 with a rework of the lower layers and a new formulation for the topside [23]. NeQuick-2 expects and input of either the solar radiation flux $F_{10.7}$ or the mean sunspot number R_{12}. The behavior of the model is only defined for values of $F_{10.7}$ in range of 63 s.f.u. to 193 s.f.u.. NeQuick-2 has been then tweaked to what is known as NeQuick-G, an official ionosphere model employed by Galileo [24] released officially in 2014. The most important difference between the two has been the parameterization of the input. NeQuick-G model input requires three coefficients that parameterize the so-called effective ionization level A_z [24]:

$$A_\mathrm{z} = a_0 + \mu_\mathrm{dip} a_1 + \mu_\mathrm{dip}^2 a_2, \tag{1}$$

where a_0, a_1, a_2 denote the aforementioned three coefficients, and μ_DIP denotes the so-called modified dip-latitude which relates the geographic latitude with the corresponding climatological magnetization level. Other differences include yet another revision of the topside ionosphere formulations and incorporation of more modern geomagnetic conditions per default.

III. Observation Model in LEO

The largest difference between the measurement error of a conventional ground receiver and a LEO-borne one, would be

the lack of the tropospheric error at LEO. Thus, we can model the GNSS observables in LEO as follows:

$$\rho_{\ell,i}^{(m)} = R_\ell^{(m)} + \delta t_\ell - \delta t_i^{(m)} + I_i^{(m)} + MP_{\rho,i} + e_i^{(m)} \quad (2)$$

$$\phi_{\ell,i}^{(m)} = R_\ell^{(m)} + \delta t_\ell - \delta t_i^{(m)} - I_i^{(m)} + MP_{\phi,i} + N_i^{(m)}\lambda_i + \eta_i^{(m)} \quad (3)$$

with

- m being m-th MEO GNSS satellite
- ℓ being ℓ-th LEO satellite
- i being i-th carrier frequency of f_i
- $\rho_{\ell,i}^{(m)}$ denoting the pseudorange observable of the m-th MEO satellite for the ℓ-th LEO satellite on i-th frequency
- $\phi_{\ell,i}^{(m)}$ denoting the carrier phase observable of the m-th MEO satellite for the ℓ-th LEO satellite on i-th frequency
- $R_\ell^{(m)}$ denoting the Euclidean distance (true range) between the position of the MEO-satellite $\boldsymbol{r}^{(m)}$ and the LEO-satellite $\boldsymbol{r}_\ell$
- $\delta t_i^{(m)}$ denoting the clock bias of the m-th MEO satellite on the i-th hardware channel in meters
- δt_ℓ denoting the clock bias of the ℓ-th LEO satellite in meters
- $I_i^{(m)}$ denoting the ionospheric delay on the i-th frequency in meters
- $MP_{\rho,i}$ denoting the multi-path error for the pseudorange observable in meters
- $MP_{\phi,i}$ denoting the multi-path error for the carrier-phase observable in meters
- $N^{(m)}$ denoting the carrier phase ambiguity in integer cycles
- λ_i denoting the wavelength of the i-th frequency f_i in meters
- $e_i^{(m)}$ denoting the receiver noise for the pseudorange observable in meters
- $\eta_i^{(m)}$ denoting the receiver noise for the carrier-phase observable in meters

The ionospheric delay term $I_i^{(m)}$ is dispersive, and thus depends on the carrier-frequency f_i. It is proportional to an integration along the signal ray path from the GNSS receiver towards the GNSS satellite. The resulting term is termed total electron content (TEC). Since this value is given for the slant ray path, we can express it as a slant TEC (STEC) from $\boldsymbol{r}_\ell$ to $\boldsymbol{r}^{(m)}$:

$$STEC^{(m)} = \int_{\boldsymbol{r}_\ell}^{\boldsymbol{r}^{(m)}} n_\mathrm{e} \mathrm{d}s, \quad (4)$$

where n_e denotes the charged particle concentration at an infinitesimally small distance of s along the ray path. Equivalently, a vertical TEC (VTEC) is given by an integration of the charged content n_e radially away from Earth along the h-height axis:

$$VTEC^{(m)} = \int_{\boldsymbol{r}_\ell} n_\mathrm{e} \mathrm{d}h, \quad (5)$$

The first-order ionospheric delay $I_i^{(m)}$ can be expressed as [20]:

$$I_i^{(m)} = \frac{K}{f_i^2} STEC^{(m)}. \quad (6)$$

Applying relevant physical constants, such as electron charge, mass, and the permittivity of free space, one can show that the index K is approximately $40.309\,\mathrm{m^3 s^{-2}}$ [20]. TEC values are often normalized to 10^{16} electrons$/\mathrm{m}^2$, and as such, are expressed in TEC units (TECU). Thus, for the GPS L1 frequency, 1 TECU is equivalent to a delay of 16.2 cm.

Without the loss of generality, let us consider an ionosphere-free combination of the GPS carrier-phase observables utilizing the L1 and L2 bands:

$$\phi_{\ell,\mathrm{IF}}^{(m)} = \frac{f_{\mathrm{L1}}^2}{f_{\mathrm{L1}}^2 - f_{\mathrm{L2}}^2}\phi_{\ell,\mathrm{L1}}^{(m)} - \frac{f_{\mathrm{L2}}^2}{f_{\mathrm{L1}}^2 - f_{\mathrm{L2}}^2}\phi_{\ell,\mathrm{L2}}^{(m)}, \quad (7)$$

where the subscript IF represents the ionosphere-free combination. Ignoring higher order terms, the ionospheric delay in L1 and L2 can be related through their frequencies as [20]:

$$I_{\mathrm{L2}}^{(m)} = \frac{f_{\mathrm{L1}}^2}{f_{\mathrm{L2}}^2} I_{\mathrm{L1}}^{(m)}. \quad (8)$$

Using Equations (3) and (7), the carrier phase ionospheric free combination can be expressed as:

$$\phi_{\ell,\mathrm{IF}}^{(m)} = R_\ell^{(m)} + \delta t_\ell - \delta t_{\mathrm{IF}}^{(m)} + MP_{\phi,\mathrm{IF}} + A_{\mathrm{IF}}\lambda_{\mathrm{IF}} + \eta_{\mathrm{IF}}, \quad (9)$$

where $\delta t_{\mathrm{IF}}^{(m)}$ denotes the ionosphere-free clock bias of the m-th GNSS satellite, $MP_{\phi,\mathrm{IF}}$ denotes the ionosphere-free multipath error, A_{IF} denotes a *non*-integer ionosphere-free ambiguity of the ionosphere-free wavelength λ_{IF}, and η_{IF} denotes the residual ionosphere-free hardware carrier-phase noise. The scaled ionosphere-free terms contain inter-frequency biases (IFB) one would like to estimate and monitor in a LEO-based GNSS monitoring application. Assuming the same noise as in a single-frequency observation, the noise σ of the L1-L2 IF observable is increased by [20]:

$$\sigma_{\mathrm{IF}} = \sigma\sqrt{\frac{f_{\mathrm{L1}}^2 + f_{\mathrm{L2}}^2}{f_{\mathrm{L1}}^2 - f_{\mathrm{L2}}^2}} = 2.02\sigma \quad (10)$$

The increase in the noise of this parameter would lead to an increase of the MDB, and thus negatively affect the effort to monitor GNSS signals. The a-priori estimation of the ionospheric delay term by utilizing the ionosphere-*only* combination, requires careful filtering and estimation of these unknown parameters, a LEO-based GNSS monitoring application would be interested in.

IV. Methodology and the Dataset

We acquire our data from publicly available databases for satellite missions. The missions which we have selected to process for this paper are a combination of missions already extensively analyzed in literature, and missions which have TEC data computed as a product. The publicity of used data makes our findings easily reproducible and comparable for the research community. The missions used in this paper are,

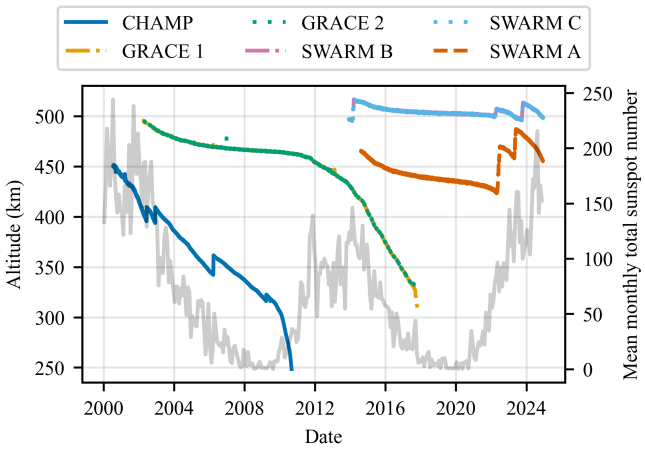

Fig. 3. Altitudes over time of LEO missions used in this paper. The altitude data have been extracted from TEC products of the respective missions and filtered for extreme outliers. Each data point is a day with mean altitude for that day. Underlaid in gray is the mean monthly total sunspot number serving as an indicator for the solar activity.

in chronological order of the launch dates: Challenging Mini Satellite Payload (CHAMP), Gravity Recovery and Climate Experiment (GRACE), and SWARM. An overview over the details of the missions is given in Table II. What's crucial is that all three missions, have equipped their satellites with a GPS receiver capable of processing both L1 and L2 bands. The particular methodology behind this estimation of the ionospheric delay from dual-frequency measurements is described by Noja et al. [25].

A. Solar flux and geomagnetic indices

At the time of writing of this paper, the data from these missions span 24 years, nearly a quarter of a century. This time frame encapsulates three distinctive solar cycles, beginning with a solar high with year 2000, and also ending with a solar high with year 2024. The solar cycles and the solar activity in general is often characterized via the number of counted sunspots. This value is often used in the form of a monthly average. Figure 3 illustrates the evolution of the mean monthly total sunspot value [26] together with the LEO missions we have selected for this paper. We use the dataset provided by Matzka et al. [27], to obtain a historical record of geomagnetic indices and solar flux observations. This dataset is used to input data into NeQuick-2 model and also to classify the resulting TEC values into timeframes with low and high solar and geomagnetic activity. The threshold value for the Ap-index is selected to be 15, as specified in Table I, the threshold value for $F_{10.7}$ has been heuristically selected to be 100 s.f.u.

B. Using NeQuick-2 and NeQuick-G

In this paper we utilize the reference implementations of NeQuick-2 and NeQuick-G, provided to us by Abdus Salam International Centre for Theoretical Physics (ICTP), and by European Union Agency for the Space Programme (EUSPA) respectively.

The coefficients of NeQuick-G have only been broadcasted and disseminated via IGS ground stations since the time of the first test satellites of Galileo in years 2013-2014. In this paper, we use the archived Galileo navigation receiver independent exchange format (RINEX) files provided by International GNSS Service (IGS) [28]. Although, these files are available from May the 5th, 2012 onwards, the NeQuick-G coefficients are changed to non-zero values from the 26th of March 2013 onwards. The stations from this dataset that have been identified to be the most consistent across the timeframe are:

- KOUR00GUF in Kourou, French Guiana,
- MAS100ESP in Maspalomas, Spain,
- REUN00FRA in Réunion, France,
- KIRU00SWE in Kiruna, Sweden,

In order to model the time before 27th of March 2013, we utilize the NeQuick-2 model, In order to circumvent the hard cutoffs present in the NeQuick-2 input checks, we have followed the guidelines specified in the source code documentation to alter the NeQuick-2 FORTRAN source accordingly. Thus, we can input solar fluxes higher than the 193 s.f.u. limit.

C. Data cleaning

Before processing the Level 2 TEC products from the satellite missions we perform various filtering and data cleaning operations to exclude outliers. This includes:

- We filter for reported altitudes deviating far too greatly from the previous altitudes, and mission nominal altitude.
- We only process measurements with carrier to noise ratio of the measured signal higher than 30 dB-Hz
- We skip epochs for which model coefficients are not available, or the reported in-site STEC values are missing
- We also filter the datasets for negative STEC values, as these are physically impossible
- We restrict all datasets to an hourly rate. We find this gives us a good balance between computational load and thoroughness. This way we still observe day-night condition changes but not at the rate of 0.1 Hz to 1 Hz.

V. Results

During the mission durations, the respective satellites in the mission have deviated from their target altitude due to orbital decay. We can see this on the visualization of the mean daily altitudes of all utilized missions in Figure 3. Thus, by analyzing data from this time frame, we not only achieve diversity in our statistics in the terms of the ionospheric disturbances caused by solar activity, but also we can explore the distribution of the STEC measurements as a function of altitude. When performing any analyses, it's important not to forget the differences in the altitudes of the missions which directly influence the topside ionospheric content a LEO satellite experiences.

We can visualize both the in-situ measured STEC values together with the NeQuick modelled ones as shown in Figure 4. An obvious observation, that can already be drawn from a glance at this dataset, suggests a frequent underestimation of the real STEC values experienced by CHAMP. Besides, a

TABLE II
OVERVIEW OF LEO MISSIONS DETAILS AND THEIR SOURCES

LEO Mission	No. of sats	Year	Nominal altitude	Data Source	Satellite Product	Dataset size
SWARM	3	2013 - ongoing	460 km to 511 km	ftp://swarm-diss.eo.esa.int	Level 2 TEC_TMS	437 GB
GRACE	2	2003 - 2017	482 km	ftp://swarm-diss.eo.esa.int	Level 2 TEC_TMS	52.9 GB
CHAMP	1	2000 - 2010	454 km	ftp://swarm-diss.eo.esa.int	Level 2 TEC_TMS	17.3 GB

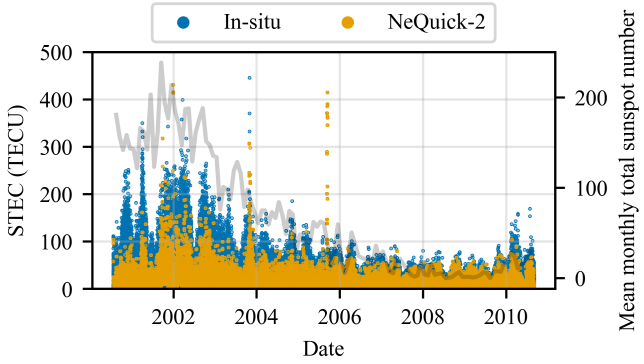

Fig. 4. Variation of the in-situ and the NeQuick-2 modelled STEC values for the duration of the CHAMP mission. Data are evaluated at an hourly rate from each day disseminated via the ESA Earth Observation portal. Underlaid in gray is the mean monthly total sunspot number.

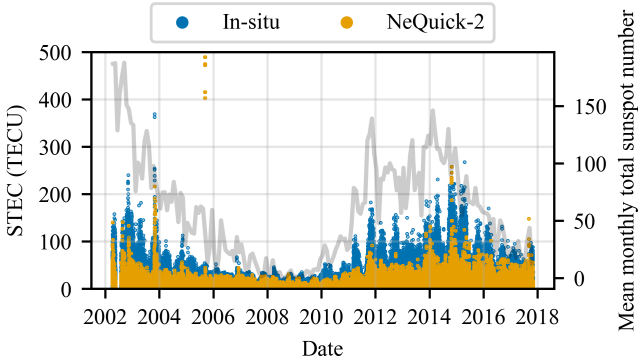

Fig. 5. Variation of the in-situ and the NeQuick-2 modelled STEC values for the duration of the GRACE mission. Data are evaluated at an hourly rate from each day disseminated via the ESA Earth Observation portal. Underlaid in gray is the mean monthly total sunspot number.

correlation between the underlaid solar cycle, represented by the mean monthly sunspot number, and the observed STEC values is visibly strong. This can be seen by the in-situ STEC values reaching as high as 300 TECU to 450 TECU during the years of high solar activity, from 2002 to 2004. The NeQuick-2 model predicts higher than usual STEC for this timeframe too, but not nearly accurate enough. In comparison, the years 2006 to 2009 were years with quite low solar activity. The STEC values, both in-situ and modelled, lay all below the 100 TECU mark for this timeframe. It is also important to note, that for these dates we can see a higher match rate between the in-situ and the NeQuick-2 reported STEC values.

Similar results can be observed for the time series data from GRACE mission as presented in Figure 5. The duration of the GRACE mission overlaps significantly with the aforementioned CHAMP mission. This was also visualized previously in Figure 3. We can see the correlation in the outliers in our data, especially the ones in late 2003, and late 2005. These peak STEC values reaching 400 TECU for CHAMP, and landing flat below the 400 TECU mark for GRACE, are primarily in-situ measured ones, strongly indicating a sudden change in the ionosphere, which has affected all three satellites, CHAMP, GRACE-1 and GRACE-2 in a same manner.

We analyze this synergy between the three satellites in more detail, by taking a closer look at the peak TEC values occurring in late 2003. The results of this analysis are presented in Figure 6. This illustrates a high correlation between the values reported by CHAMP and GRACE-1 and GRACE-2. On average, we can also observe the reported in-situ STEC

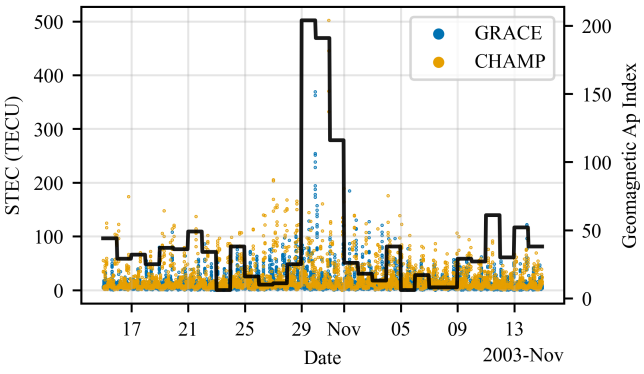

Fig. 6. Close-up on the extremely high in-situ STEC measurements consistently observed across CHAMP, GRACE-1 and GRACE-2 satellites. The outliers are correlated to the extreme geomagnetic storm events in late 2003 as also indicated by the geomagnetic Ap index in black.

values of the GRACE mission to be lower of those from the CHAMP mission. This is expected, for the entire duration of the both missions, GRACE satellites flew higher than CHAMP, and thus were exposed to less electron content of the F-region. The extreme geomagnetic storm from the 29th to the 30th of November 2003, show us nevertheless, that the STEC variation does occur no matter the altitude difference.

Different to the previous two missions, we can utilize the NeQuick-G model for the SWARM mission, as for the entirety of its timeframe we are able to extract Galileo navigation message coefficients for the effective ionization level. The SWARM mission is ongoing as of writing of this paper. The

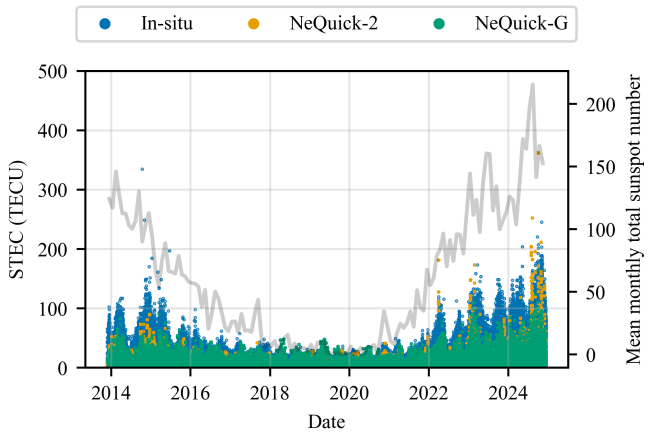

Fig. 7. Comparison of the in-situ, NeQuick-G, and the NeQuick-2 STEC values for the duration of the SWARM mission. Data are evaluated from all three satellites (A, B, C) at an hourly rate from each day disseminated via the SWARM data portal. Underlaid in gray is the mean monthly total sunspot number.

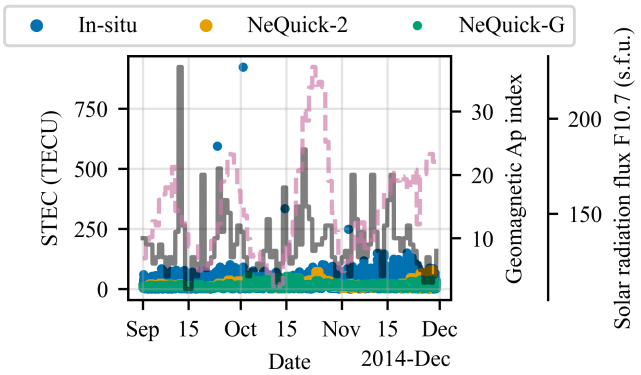

Fig. 8. Detailed look into the outliers of the SWARM A data occurring in late 2014. The extreme in-situ values are correlated with high solar flux (magenta) and high geomagnetic activity (black).

latest data we have obtained in the preparation of the data analysis has been the 14th December 2024. The time series of the STEC values measured by the three SWARM satellites are presented in Figure 7. As with the previous missions, a clear correlation between the STEC values and the solar radiation can be observed on a global scale. We can see pretty close performance of NeQuick-G and NeQuick-2 in modelling the STEC values during the low solar activity period between the years 2018 and 2020. For the recent years with increased of solar activity, we can start no notice a few outliers. Those are primarily coming from the NeQuick-2 model. Different to the previous two missions, SWARM satellite B sits at highest among all satellites in this paper, at around 500 km. This might be a contributing factor to the mismatches, due to a dated formulation of the topside in NeQuick-2 in comparison to NeQuick-G. NeQuick-G also relies on real-time reporting from reference stations, which are then passed through the Galileo ground segment. This might suggest the better quality of the reported estimates.

Data from the SWARM satellite A contains unusual peaks in the reported in-situ STEC values from year 2014 on October 10th. We have filtered those the extreme outliers from Figure 7 but present those in detail in Figure 8. As we can see, these events are also correlated either with heightened observed solar flux $F_{10.7}$ or heightened geomagnetic activity parameterized via the Ap index. The reported outliers reach as high as 800 TECU. These outliers are also mismodeled by both NeQuick-G and NeQuick-2, as the models do not anticipate such sudden changes in the ionosphere.

A. May 2024 solar and geomagnetic storm

Our dataset contains what has become known to be the greatest solar storm in recent times since 1989, taking place between the 10th to 12th May 2024 [29]. The extreme geomagnetic conditions ionized the upper layers of the atmosphere so much that Aurora Borealis were visible over most of Europe, North America, with some observations coming as close to the equator as from Canary Islands, Guatemala, Namibia, and Oman.

Different from our other analyses which use hourly sampled data, we have explicitly analyzed the raw 1Hz data from the SWARM mission, to better understand the dynamics of the topside ionosphere during this geomagnetic event. In order to map the ionospheric conditions during the day, we utilize the VTEC values provided in the satellite products. This is a value estimated from STEC values. The relation between STEC and VTEC is modelled by so-called the *mapping functions* in relevant literature. We use the one derived for SWARM data by Montenbruck and González Rodríguez [17] based on the more general Foelsche and Kirchengast (F&K) mapping function [30] given here as:

$$VTEC = STEC \frac{2.087}{\sqrt{\sin^2(\theta) + 0.076} + \sin(\theta)}, \qquad (11)$$

where θ denotes the elevation angle in the local tangential coordinate system of the receiver towards the slant path.

We apply this Equation (11) to predicted STEC values by NeQuick-G and NeQuick-2 in order to create predicted VTEC values to compare to in-situ VTEC values. By following the guidance of the SWARM data product handbook, for each epoch we select the GPS satellite that has had the highest elevation. This GPS satellite is selected to have the best possible in-situ measurement of the VTEC value. The comparison between the provided in-situ VTEC values and the predicted NeQuick-G ones is given in Figure 9. The illustration shows the ground tracks of all three SWARM satellites compounded in the timeframe between the 10th and 12th of May 2024. The Figure 9(a) illustrates the VTEC in-situ values, whereas Figure 9(b) and Figure 9(c) illustrate the NeQuick-2 and NeQuick-G modelled VTEC respectively. All illustrated values of VTEC are median values that are collected on a grid of 1° latitude by 3° longitude tiles.

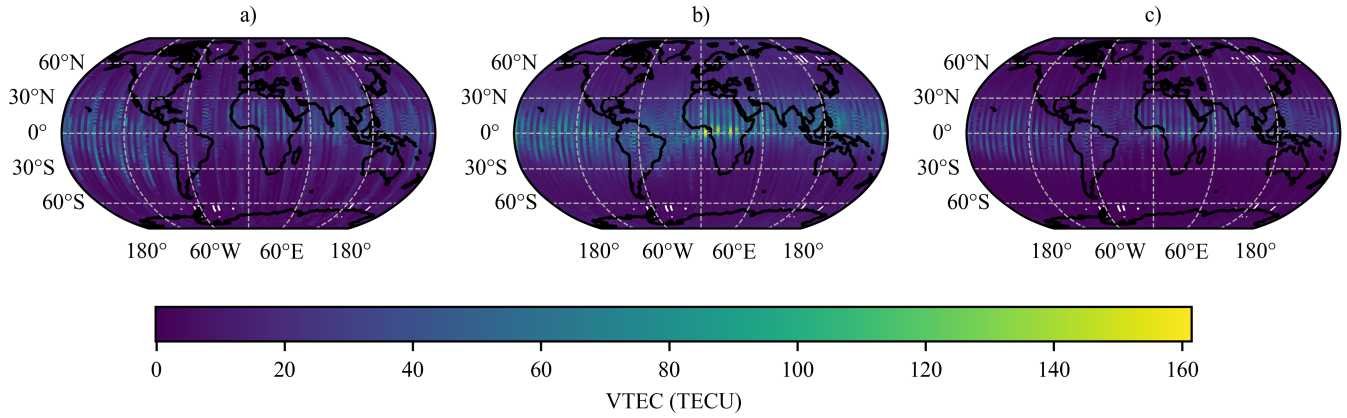

Fig. 9. Compounded in-situ VTEC (a), NeQuick-2 VTEC (b), and NeQuick-G VTEC (c) from SWARM A, B, C ground tracks on solar storm peak days between May 10th and 12th in 2024. For each epoch a satellite with the highest elevation is taken for the VTEC value. Median VTEC fills a 1° latitude by 3 degree longitude tile.

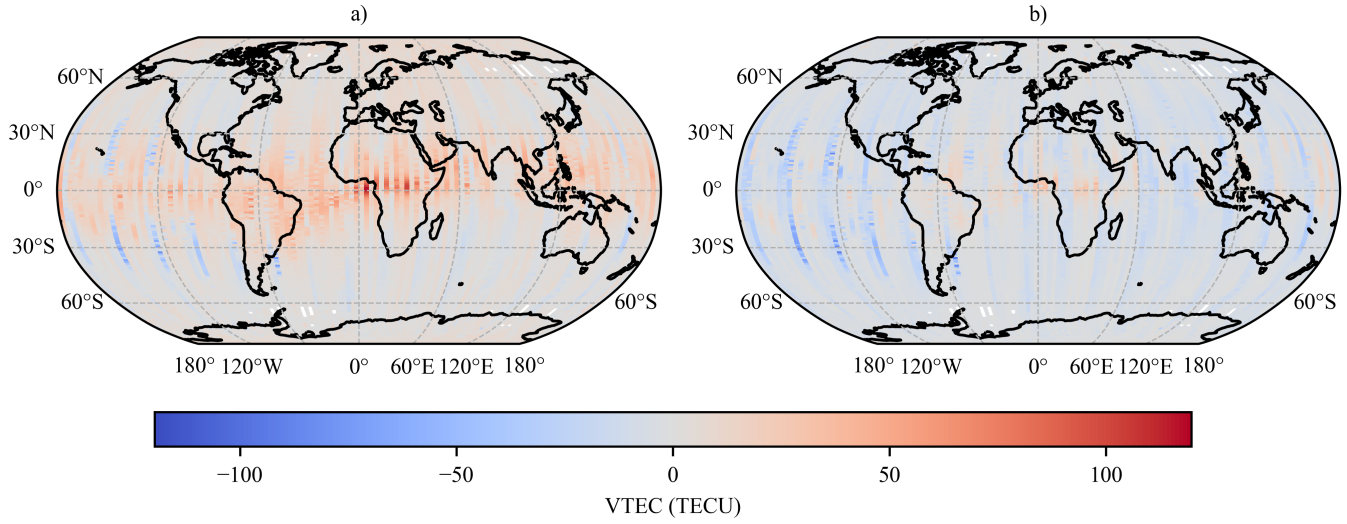

Fig. 10. Difference between median in-situ VTEC from SWARM A, B, C and two models: NeQuick-2 (a) and NeQuick-G (b). Positive values indicate overestimation, negative ones underestimation. The data are compounded over solar storm peak days between May 10th and 12th in 2024. Each tile stretches 1° latitude by 3 degree longitude.

As one can immediately recognize, the topside ionosphere has not suffered as great of an ionization as NeQuick-2 predicts. NeQuick-G seems to do a better job at predicting the stormy event. This is especially clear, upon closer inspection of Figure 10 which represents the differences between the measured and modeled median VTEC values. Positive values indicate overestimation, negative ones underestimation. Figure 10(a) and Figure 10(b) illustrate these differences for predicted median VTEC values for NeQuick-2 and NeQuick-G respectively. Most equatorial regions suffer from overestimation by NeQuick-2 of around 50 TECU to 100 TECU. As stated previously, NeQuick-G seems to outperform NeQuick-2 here, by having reduced the overestimation regions to equatorial Africa and northern coasts of South America. The amount of the overestimation seems to be less extreme as well, bound to be between 0 TECU to 50 TECU.

B. *Model discrepancy*

In order to quantify and analyze the mismatch between the in-situ STEC values and the modelled ones via NeQuick we define a simple discrepancy metric. We compare values that are related to the same epoch. For this case, we specifically decide against metrics that ignore the sign of the skew of the error, such as the widely used root-mean-squared-error (RMSE) metric. Instead, we define the discrepancy as a simple difference as follows:

$$\Delta = TEC_{\text{model}} - TEC_{\text{in-situ}} \tag{12}$$

where Δ denotes the discrepancy. Thus, the defined discrepancy metric constitutes the residual error we have set out to

investigate. In the following we will quantify the discrepancy using statistical characterization. Therefore, we will utilize the statistical mean, median, and the standard deviation of the differences between the model and in-situ measurements.

For a model that acts conservatively, and as such provides an overbound to in-situ measurements, we would thus expect the following relation to hold:

$$\mathrm{E}(\Delta) > 0, \tag{13}$$

where $\mathrm{E}(\cdot)$ denotes the statistical notion of the expected value. Ideally, our model would also be accurate enough to represent the underlying data so that the standard deviation $\mathrm{std}(\Delta)$ would be as small as possible.

As mentioned previously, it is important to make sure not to lose the context of the altitude when analyzing the integrated TEC. We have visualized the relationship between the altitude and VTEC values of from all mission datasets in Figure 11. In Figure 11(a), we only include VTEC values reported by observables of elevation degree $\theta > 50°$ as recommended by SWARM L2 Product Handbook [31].

We apply this mapping function to NeQuick-2 modelled STEC values across the entire dataset and visualize the resulting VTEC in Figure 11(b). In order to visualize the difference between in-situ and modelled VTEC, we visualize the discrepancy Figure 11(c) using Equation (13). For all statistics we provide a median and a 95-th percentile line across the altitudes.

To analyze the performance of the models in general, we group the STEC values into four categories that relate to the state of the ionosphere:

- low solar flux *and* low geomagnetic activity (nominal case)
- low solar flux *but* high geomagnetic activity
- high solar flux *but* low geomagnetic activity
- high solar flux *and* high geomagnetic activity (non-nominal case)

Thus, we can evaluate the metrics such as $\mathrm{E}(\Delta)$ or $\mathrm{std}(\Delta)$ under assumptions of nominal and non-nominal conditions. This is a standard procedure in evaluation the error sources and their distribution in the context of integrity monitoring in GNSS.

We have visualized the discrepancy between the CHAMP in-situ STEC values and NeQuick-G estimated STEC in Figures 12 and 13, and are going to discuss the implications of the resulting discrepancies in the next section.

VI. Discussion

Our analysis of residual TEC in the topside ionosphere agrees with existing literature in the topic. In general, Figures 4, 5 and 7, confirm a non-negligible amount of charged content in the upper layers of the ionosphere. We found in Figure 11(a), that even the highest in-situ measurements from the SWARM-C satellite orbiting above 500 km demonstrate STEC values reaching from 100 TECU to 200 TECU. The reported residual error of 4 m in CHAMP dataset by Montenbruck and Gill [15] roughly corresponds to our findings applied

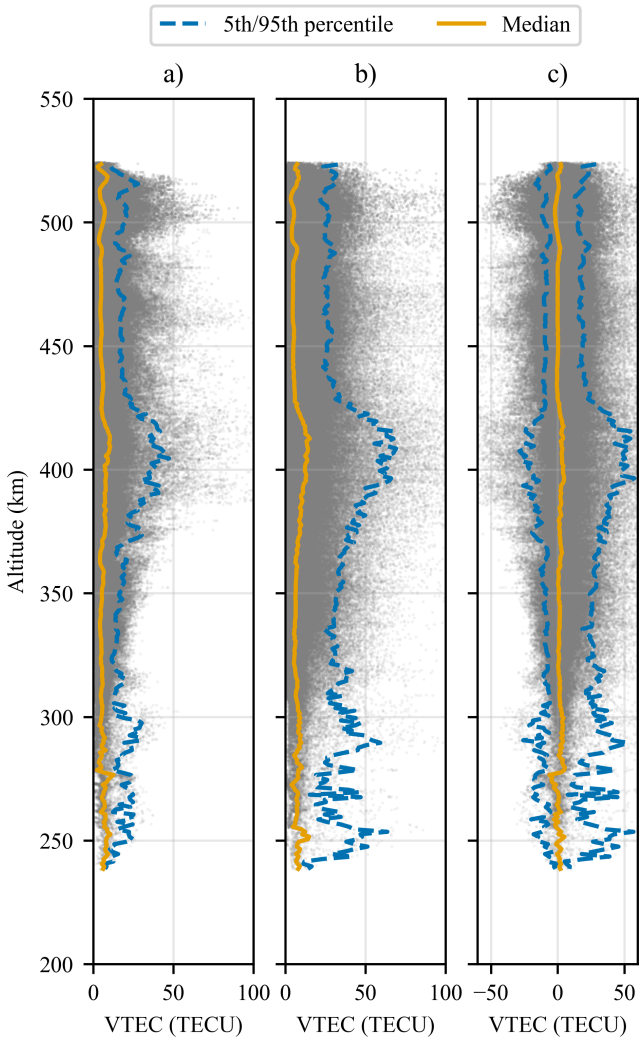

Fig. 11. Comparison between in-situ VTEC values (a), and NeQuick-2 VTEC values (b) with respect to the altitude. The difference (b) - (a) between the two is visualized in (c). Gray points are VTEC values gathered from SWARM (A, B, C), GRACE (1, 2) and CHAMP satellites. The blue dashed line represents the (5th) 95th percentile of the VTEC value at a certain altitude. The yellow solid line the median VTEC.

to all datasets in Figure 12(c), if we consider the computed standard deviation of around 28 TECU being equivalent to 4.5 m of pseudorange error for GPS L1. Comparing the results in Figure 12, we can confirm the observations of Montenbruck and González Rodríguez [17], that low solar activity epochs have a higher probability for correctly predicting and thus correcting for ionospheric delays.

We find it interesting to highlight the volatility of the topside on the example of Figure 6. At the peak of the geomagnetic storm in late 2003, we see the values reported by the GRACE satellites at some points exceeding those coming from CHAMP. This is particularly peculiar as for the same timeframe GRACE satellites are at around 475 km orbital altitude, and the CHAMP satellite just flat of 400 km.

With regard to the existing 3D-ionospheric models, our anal-

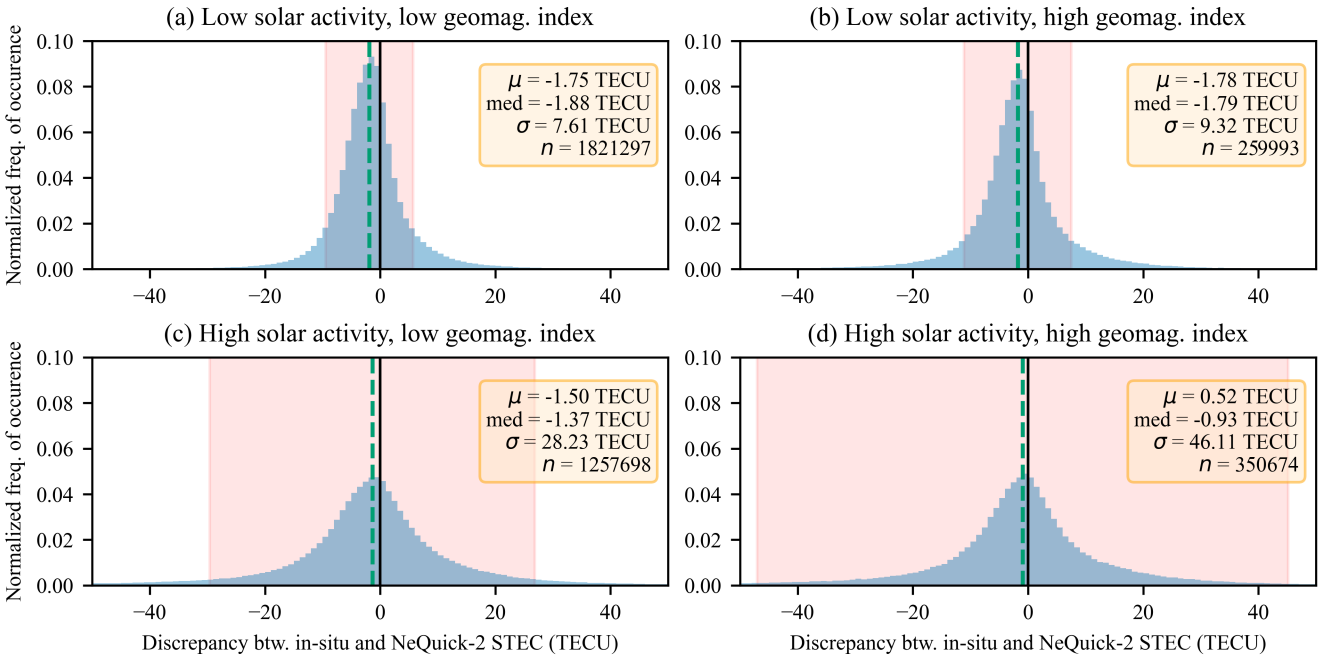

Fig. 12. Discrepancy between in-situ and NeQuick-2 STEC values for SWARM A, B, C, GRACE-1, GRACE-2, CHAMP missions. Grouping is done into solar radiation level and geomagnetic activity. The orange boxes report the mean μ, median, the standard deviation σ of the discrepancy. Number of points used to generate the statistic is provided under n. The magenta tinted area indicates the standard deviation of the distribution.

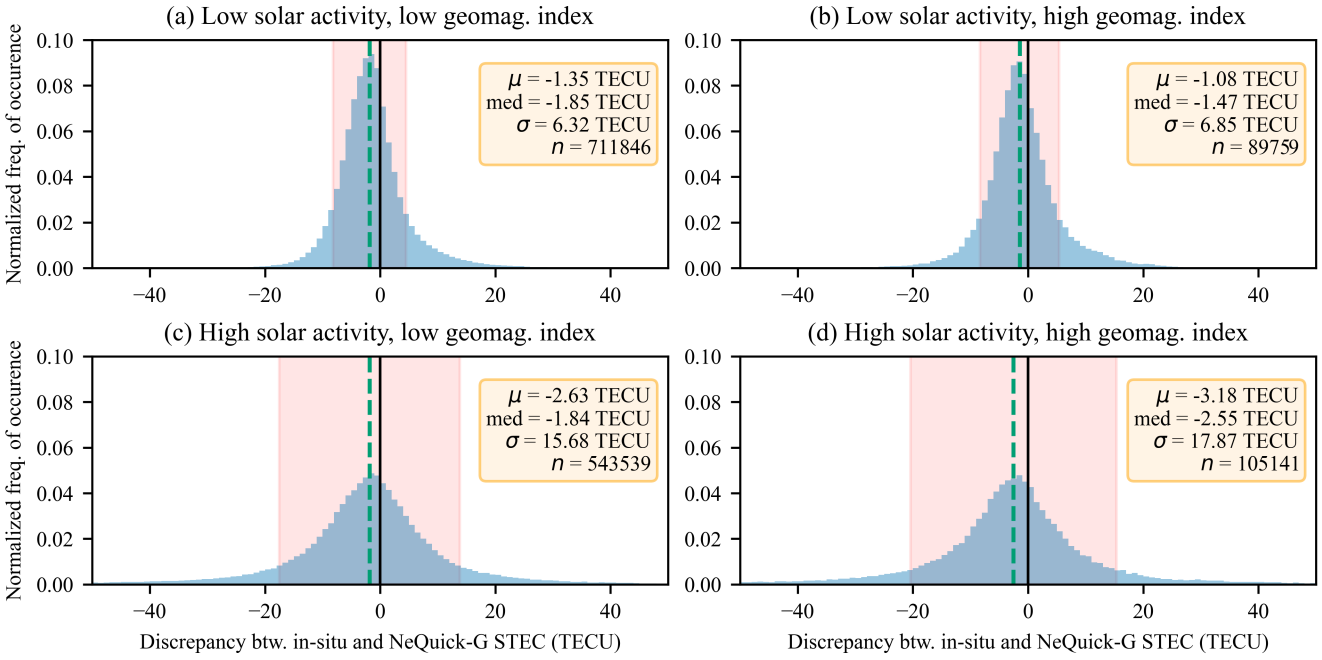

Fig. 13. Discrepancy between in-situ and NeQuick-G STEC values for SWARM A, B, C. Grouping is done into solar radiation level and geomagnetic activity. The orange boxes report the mean μ, median, the standard deviation σ of the discrepancy. Number of points used to generate the statistic is provided under n. The magenta tinted area indicates the standard deviation of the distribution.

yses indicate decent performance under nominal ionospheric conditions of both NeQuick-2 and NeQuick-G. Between the two, the results in Figure 9(b) and Figure 9(c), and especially those presented in Figure 13(a) indicate a slight preference for NeQuick-G. We would like to also highlight that NeQuick-G can easily be used in LEO application, since the coefficients for the model are broadcast by Galileo.

If we interpret the statistical parameters from Figures 12 and 13 in terms of the pseudorange error, there are some important limitations we can highlight. For the nominal conditions the median discrepancy results in around 30 cm, with a standard deviation of around 1.02 m to 1.23 m. The over 1 m standard deviation of it definitely overshoots any MDB targets that are set for hardware bias term estimating in GNSS, as these are in close to 30 cm to 50 cm error in pseudorange. As such, this residual added noise from the mismatch of the observed and modeled ionospheric delay would saturate the parameters one would monitor in a LEO-based GNSS monitoring scenario. Non-nominal conditions, such as solar and geomagnetic storms present a challenge for the models. This as well, though, is expected to some extent, as the models aim to reflect the median (climatological) behavior. We have shown this in Figure 11(c), where the median discrepancy stays at or around the 0 TECU mark. In the same Figure 11(c), the range between the 5-th and 95-th percentile, seems to widen around the 400 km which roughly corresponds to the F-region peak, and thus might induce some instability in the model. The lower end of the altitudes also show quite an erratic behavior of the bounds. We believe the source of its might be twofold: these altitudes only have few measurements coming from CHAMP towards its end of mission. Also, the used mapping function Equation (11) might be in the need of a tweak to accommodate another range of altitudes this low.

Nevertheless, the increased uncertainties are highly visible Figure 12(c) - (d), TEC. Although the median deviation is increased only to 2.55 TECU, the standard deviation is in the range of 17.9 TECU to 46.1 TECU corresponding to an uncorrected L1 pseudorange error of 2.9 m to 7.5 m. In addition, all the positional parameters, such as the median and the mean, Figures 12 and 13 (a) - (d) have a negative sign in front if them. This indicates a skew towards the "optimistic" case, meaning the models on average underestimate the in-situ values in LEO.

The focus on the three scientific missions presented in this paper has had advantages, such as the assurance that all missions have used the same methodology to derive the STEC values. Also, we value the ease of access of the publicly available data from these missions, that span 24 years, making our finding even more reproducible. However, the selection of the satellites also limits some of our findings. Especially considering the altitude diversity, the considered LEO missions all occupy a low Earth orbit of around 300 km to 500 km nominally. Compared to the LEO missions target altitudes additionally occupying the higher LEO range of 600 km to 1500 km, our analyzed altitudes might suffer from more ionospheric error than missions situated higher. Another limiting factor for the analyzed in-situ values has been the source of the STEC values. Though these are precise, coming from carrier-phase GPS observations, an analysis of TEC measurements from Langmuir probes and/or radio occultation data could potentially widen the applicability of the methodology we applied in this paper. In our future work we would like to also examine other 3D-ionospheric models, and find tighter bounds on the residual ionosphere for LEO-borne receivers.

VII. Conclusion

In this work we have aimed to quantify the expected residual ionospheric error in LEO with a direct application for future LEO applications: LEO PNT and LEO-based GNSS monitoring. Our analysis of the in-situ TEC from LEO satellite products agrees with the current understanding of the ionosphere, and indicates drop in the electron content after the F-region peak. Thus, LEO missions carrying a GNSS receiver should experience significantly lower ionospheric error above 400 km.

We have compared the in-situ TEC with TEC predicted via 3D-ionospheric models such as NeQuick-2 and NeQuick-G. Our findings indicate decent performance of the models across all studied altitudes. We found a slight preference for NeQuick-G, as it consistently outperformed NeQuick-2 and also is ready to be used in space relying only on Galileo broadcast message.

The median deviation from in-situ measurements was found to be around 1.8 TECU. In nominal cases the residual uncorrected error of the models has a standard deviation of 6.3 TECU to 7.6 TECU, which corresponds to 1 m to 1.2 m error of GPS L1 pseudorange. Under non-nominal conditions the models deviate highly from the observed TEC. Although the median deviation is increased only to 2.55 TECU, the standard deviation is in the range of 17.9 TECU to 46.1 TECU corresponding to an uncorrected L1 pseudorange error of 2.9 m to 7.5 m.

More research is required to tighten this bound on the error induced by the residual ionosphere in LEO. Combining different approaches, such as combinations of observables together with more accurate models of the ionosphere might provide an even more accurate correction for this error. This would be highly needed for the LEO-based GNSS monitoring application, as the residual errors after applying the model still do not provide required sensitivity for monitoring of hardware biases of GNSS satellites.

Acknowledgment

We would like to thank the Abdus Salam International Centre for Theoretical Physics (ICTP), especially Dr. Bruno Nava for providing the source code of the International Telecommunications Unit (ITU) NeQuick-2 model. We would also like to thank the EUSPA for granting us access to the source code of the NeQuick-G reference implementation authored by the European Commission's Joint Research Center (JRC).

References

[1] Z. M. Kassas et al., "Navigation with Multi-Constellation LEO Satellite Signals of Opportunity: Starlink, OneWeb, Orbcomm, and Iridium," in *2023 IEEE/ION Position, Location and Navigation Symposium (PLANS)*, Apr. 2023, pp. 338–343. DOI: 10.1109/PLANS53410.2023.10140066.

[2] B. Eissfeller, T. Pany, D. Dötterböck, and R. Förstner, "A Comparative Study of LEO-PNT Systems and Concepts," in *Proceedings of the ION 2024 Pacific PNT Meeting*, Honolulu, Hawaii, May 8, 2024, pp. 758–782. DOI: 10.33012/2024.19646.

[3] Ries, Lionel et al., "LEO-PNT for Augmenting Europe's Space-based PNT Capabilities," in *2023 IEEE/ION Position, Location and Navigation Symposium (PLANS)*, Monterey, California: IEEE, Apr. 25, 2023.

[4] T. G. Reid et al., "Satellite Navigation for the Age of Autonomy," in *2020 IEEE/ION Position, Location and Navigation Symposium (PLANS)*, Apr. 2020, pp. 342–352. DOI: 10.1109/PLANS46316.2020.9109938.

[5] P. Anderson, G. Schmitt, F. Ahmed, and P. Shannon, "A New Paradigm of Commercial GNSS Services: The Case for LEO PNT at C-Band, Part 1," in *Proceedings of the 37th International Technical Meeting of the Satellite Division of The Institute of Navigation (ION GNSS+ 2024)*, Baltimore, Maryland, Oct. 9, 2024, pp. 2250–2271. DOI: 10.33012/2024.19671.

[6] W. Li et al., "LEO augmented precise point positioning using real observations from two CENTISPACE™ experimental satellites," *GPS Solutions*, vol. 28, no. 1, p. 44, Dec. 12, 2023, ISSN: 1521-1886. DOI: 10.1007/s10291-023-01589-0.

[7] T. Zechel, "GNSS Augmentation Satellite System (GAUSS)," presented at the ION GNSS+ 2024 (Baltimore, USA), Sep. 20, 2024.

[8] W. Gao et al., "Initial Design for Next-Generation BeiDou Integrity Subsystem: Space–Ground Integrated Integrity Monitoring," *Remote Sensing*, vol. 16, no. 22, p. 4333, 22 Jan. 2024, ISSN: 2072-4292. DOI: 10.3390/rs16224333.

[9] O. García Crespillo, M. Meurer, C. Oezmaden, and M. Brachvogel, "Integrity Monitoring and Augmentation of GNSS from Low Earth Orbit Constellations," in *Proceedings of the 37th International Technical Meeting of the Satellite Division of the Institute of Navigation*, Baltimore, USA, 2024.

[10] T. P. Yunck, "Orbit Determination," in *Global Positioning System—Theory and Applications, Vol. 2*, vol. 2, 2 vols., Washington DC: American Institute of Aeronautics and Astronautics, Jan. 1, 1996, pp. 559–592, ISBN: 978-1-56347-107-0 978-1-60086-639-5.

[11] J. Klobuchar, "Ionospheric Time-Delay Algorithm for Single-Frequency GPS Users," *IEEE Transactions on Aerospace and Electronic Systems*, vol. AES-23, no. 3, pp. 325–331, May 1987, ISSN: 0018-9251. DOI: 10.1109/TAES.1987.310829.

[12] X. Ren, J. Chen, X. Zhang, M. Schmidt, X. Li, and J. Zhang, "Mapping topside ionospheric vertical electron content from multiple LEO satellites at different orbital altitudes," *Journal of Geodesy*, vol. 94, no. 9, p. 86, Aug. 18, 2020, ISSN: 1432-1394. DOI: 10.1007/s00190-020-01415-2.

[13] L. Schreiter et al., "Topside Ionosphere Sounding From the CHAMP, GRACE, and GRACE-FO Missions," *Radio Science*, vol. 58, no. 3, e2022RS007552, Mar. 2023, ISSN: 0048-6604, 1944-799X. DOI: 10.1029/2022RS007552.

[14] L. Schreiter, A. Brack, B. Männel, H. Schuh, D. Arnold, and A. Jäggi, "Imaging of the Ionosphere and Plasmasphere Using GNSS Slant TEC Obtained From LEO Satellites," *Radio Science*, vol. 59, no. 12, e2024RS008058, 2024, ISSN: 1944-799X. DOI: 10.1029/2024RS008058.

[15] O. Montenbruck and E. Gill, "Ionospheric Correction for GPS Tracking of LEO Satellites," *Journal of Navigation*, vol. 55, no. 2, pp. 293–304, May 2002, ISSN: 0373-4633, 1469-7785. DOI: 10.1017/S0373463302001789.

[16] J. Kim and M. Kim, "Determination of Ionospheric Delay Scale Factor for Low Earth Orbit using the International Reference Ionosphere Model," *Korean Journal of Remote Sensing*, vol. 30, no. 2, pp. 331–339, Apr. 30, 2014, ISSN: 1225-6161. DOI: 10.7780/kjrs.2014.30.2.14.

[17] O. Montenbruck and B. González Rodríguez, "NeQuick-G performance assessment for space applications," *GPS Solut.*, vol. 24, no. 1, Nov. 19, 2019, ISSN: 1080-5370. DOI: 10.1007/s10291-019-0931-2.

[18] J. Kim and M. Kim, "NeQuick G model based scale factor determination for using SBAS ionosphere corrections at low earth orbit," *Advances in Space Research*, vol. 65, no. 5, pp. 1414–1423, Mar. 2020, ISSN: 02731177. DOI: 10.1016/j.asr.2019.11.038.

[19] M. Imad, A. Grenier, X. Zhang, J. Nurmi, and E. Lohan, "Ionospheric Error Models for Satellite-Based Navigation—Paving the Road towards LEO-PNT Solutions," *Computers*, vol. 13, no. 1, p. 4, Dec. 22, 2023, ISSN: 2073-431X. DOI: 10.3390/computers13010004.

[20] P. J. Teunissen and O. Montenbruck, Eds., *Springer Handbook of Global Navigation Satellite Systems*, 1st ed. Springer International Publishing, 2017, 1268 pp., ISBN: 978-3-030-73172-4.

[21] L. R. Cander, *Ionospheric Space Weather* (Springer Geophysics). Cham: Springer International Publishing, 2019, ISBN: 978-3-319-99330-0 978-3-319-99331-7. DOI: 10.1007/978-3-319-99331-7.

[22] G. Di Giovanni and S. M. Radicella, "An analytical model of the electron density profile in the ionosphere," *Advances in Space Research*, vol. 10, no. 11, pp. 27–30,

Jan. 1, 1990, ISSN: 0273-1177. DOI: 10.1016/0273-1177(90)90301-F.

[23] B. Nava, P. Coïsson, and S. M. Radicella, "A new version of the NeQuick ionosphere electron density model," *Journal of Atmospheric and Solar-Terrestrial Physics*, Ionospheric Effects and Telecommunications, vol. 70, no. 15, pp. 1856–1862, Dec. 1, 2008, ISSN: 1364-6826. DOI: 10.1016/j.jastp.2008.01.015.

[24] European commission, "European GNSS (Galileo) Open Service - Ionospheric Correction Algorithm for Galileo Single Frequency Users," 2014.

[25] M. Noja, C. Stolle, J. Park, and H. Lühr, "Long-term analysis of ionospheric polar patches based on CHAMP TEC data," *Radio Science*, vol. 48, no. 3, pp. 289–301, 2013, ISSN: 1944-799X. DOI: 10.1002/rds.20033.

[26] SILSO World Data Center, *The International Sunspot Number*, Royal Observatory of Belgium, avenue Circulaire 3, 1180 Brussels, Belgium, 2000–2024.

[27] J. Matzka, O. Bronkalla, K. Tornow, K. Elger, and C. Stolle, *Geomagnetic Kp index*, version 1.0, GFZ Data Services, 2021. DOI: 10.5880/KP.0001.

[28] International GNSS Service (IGS), *Daily 30-Second GNSS Observation Data*, RINEX, NASA Crustal Dynamics Data Information System, 1992. DOI: 10.5067/GNSS/GNSS_DAILY_O_001.

[29] H. Hayakawa et al., "The Solar and Geomagnetic Storms in 2024 May: A Flash Data Report," *The Astrophysical Journal*, vol. 979, no. 1, p. 49, Jan. 2025, ISSN: 0004-637X. DOI: 10.3847/1538-4357/ad9335.

[30] U. Foelsche and G. Kirchengast, "A simple "geometric" mapping function for the hydrostatic delay at radio frequencies and assessment of its performance," *Geophysical Research Letters*, vol. 29, no. 10, pp. 111-1-111–4, 2002, ISSN: 1944-8007. DOI: 10.1029/2001GL013744.

[31] Swarm Expert Support Laboratories, "Swarm L2 TEC Product Description," Product Description SW-TR-GFZ-GS-0007, May 22, 2017, p. 15.